IEEE Robotics and Automation Letters (RAL) paper presented at the
2020 IEEE/RSJ International Conference on Intelligent Robots and Systems (IROS)
October 25-29, 2020, Las Vegas, NV, USA (Virtual)

Bilateral humanoid teleoperation system using whole-body exoskeleton cockpit TABLIS

Yasuhiro Ishiguro[1] and Tasuku Makabe[1] and Yuya Nagamatsu[1] and Yuta Kojio[1] and Kunio Kojima[1] and Fumihito Sugai[1] and Yohei Kakiuchi[1] and Kei Okada[1] and Masayuki Inaba[1]

***Abstract*— We describe a system design approach for the bilateral teleoperation of a humanoid robot. We have focused on bipedal stability and 2D/3D locomotion space problems. Our proposed system has two robot hardware and two control software. The master side hardware is newly developed seat-type whole-body exoskeleton cockpit called "TABLIS", and the master side software reproduces a remote 2D/3D ground surface and overcomes the space limitation of locomotion, such as the use of treadmills. The slave side software prevents the humanoid from falling down in cases where an operator provides an inaccurate input. We used humanoid robot "JAXON" as a slave side hardware. We have demonstrated a bilateral quasi-3D step traversing and the validity of our system design.**

I. Introduction

The teleoperation of a whole-body humanoid has several challenges. In case of an upper-half humanoid robot, the lower body mechanisms are either composed of a cart-type machine or fixed to the ground. Therefore, the main concern, in this case, is the kinematics or statics, such as inverse kinematics, collision avoidance, and touch haptics. On the other hand, the main concern in the case of whole-body humanoid robots are the dynamics of their bipedal body. Its dynamics is naturally unstable and often modeled as a linear inverted pendulum (LIP) model. In terms of an online real-time teleoperation, the robot has to track the sequential input of the operator while conforming to several dynamics constraints. Owing to these difficulties, a normal operator cannot maneuver the whole-body humanoid directly. Therefore, we have developed an assistive software approach to maneuver the bipedal dynamics [1]. While conducting locomotion teleoperation, the operator has to deal with limitations of the available space. This is because the locomotion of the robot depends on the operator's movements; for example: to enable the robot to walk around, the operator should also walk around. To mitigate this limitation, a mechanism, such as a treadmill, is required. However, the humanoid robot should act in the 3D real world and interact using its whole-body. Thus, those limitations cannot be overcome using the existing devices. Our proposed system has unique bipedal-oriented software systems and a cockpit-like whole-body hardware device and enables 3D bipedal teleoperation, as Fig. 1.

II. Related works

A. Hardware interface design for humanoid teleoperation

Fig. 2 shows the different candidate hardware interface device designs for conducting the teleoperation of the whole-body humanoid robot. (a) is a standing human with a motion capture device. This is the most popular and simple approach for humanoid motion transfer. Researchers often use some vibration/pressure haptic devices to feedback tactile sensing or bipedal balancing [2]. However, the reproducibility of the physical interaction and the locomotion workspace is limited. (b) is a commercial virtual reality (VR) gaming device that provides an infinite floor exploration using slip walking, and this can be used as a humanoid locomotion interface [3]. However, there is no force feedback, and it is difficult to extend this design to 3D locomotion. (c) is a 2D treadmill device that provides an infinite floor exploration through natural walking [4]. However, there is no force feedback, and it cannot be applied to 3D locomotion. (d) has two force or position feedback devices facing the operator's sole and these provide infinite 3D locomotion similar to a 3D treadmill [5]. The disadvantage of this design is that its use is mainly limited to locomotion, and standing, using this device, is more stressful than being seated. (e) is a set of 3D haptic devices facing towards the two end-effectors on the operator's side and provides force feedback on every end-effector [6]. Similar to the design shown in (d), the opposed device placement impedes the range of the operator's whole-body motion. (f) is an exoskeleton type device that provides dual-arm force feedback and is often applied in teleoperation [7]. Conventional humanoid robot teleoperation mainly focuses on the upper body, while the lower body control method consists of simple pedal devices or slip walking. (g) is a seat-type whole-body exoskeleton cockpit, which has

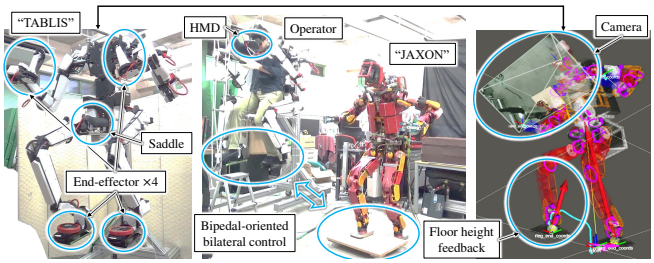

Fig. 1. Images of the seat-type whole-body exoskeleton cockpit "TABLIS" and a bilateral quasi-3D locomotion performed by the robot JAXON.

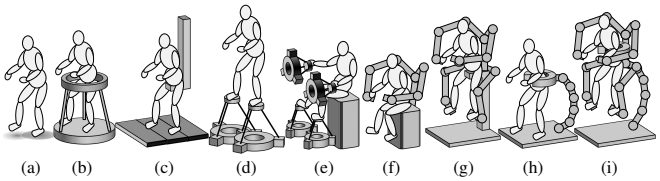

Fig. 2. Different device designs for whole-body humanoid teleoperation.

[1] Graduate School of Information Science and Technology, The University of Tokyo, Japan

Copyright ©2020 IEEE

been adopted in this work. This could be explained as the extension of the device shown in (f). The operator's base link (waist) is fixed on the saddle seat, similar to that of a bicycle. As a result, only near-standing or sitting motion transfer is available. Its human-like serial link chain provides enough workspace and extensibility to activities such as car driving, high kicking, and ladder climbing. This device has several advantages; it enables efficient 2D/3D locomotion, allows whole-body workspace, and causes less stress during long-time operations. The installation area could be up to a size larger than humans. The disadvantages are the expensive fully actuated joint system and reduced stiffness/precision, compared with the parallel link joint devices. (h) is a standing human with a force feedback mechanism on his waist. Basically, the whole-body motion of the operator is captured the same as (a), and the force feedback function to the COM/waist of the operator provides a direct bilateral synchronization of the bipedal dynamics [8], [9]. (i) is a more complex whole-body exoskeleton device concept and can be explained as the combination of the (g) and (h). This system has an analogy to the human's whole-body kinematics model with a floating base link. The 6 degrees-of-freedom (DOF) actuated base link can overcome the limitation of the operator's waist pose in (g) and can enable the operation of crawling/lying or a more intuitive 2D/3D locomotion with base link acceleration. However, the root joint actuator system will require over 150 kg load capacity, similar to a heavy industrial robot arm, and its installation space and cost would be excessive for daily use.

B. *Software design for bipedal teleoperation*

Conventional bipedal teleoperation studies can be reorganized in terms of the abstraction level of the bipedal locomotion command. While using a high-level abstract command, the operator mainly inputs footsteps [10] or overall movement direction [11], [3]. Certain gait generation programs, based on predictive control, quadratic programming, or capture point, generate a detailed whole-body joint motion. This approach can provide higher stability due to its well-planned gait, however, it is difficult to control its 6-DOF foot position manually. Therefore, maneuverability tends to be lower in such cases.

While using a middle-level abstract command, the operator inputs their foot/COM force/position directly. However, certain motion modification programs modify the input motion to satisfy the constraints of bipedal dynamics [12], [1]. The operator is allowed to control their COM/feet motion manually, but their detailed trajectories are modified online. Therefore, this approach provides medium maneuverability as well as stability. Our approach in this work is also categorized to be of this type.

While using a low-level abstract command, the operator inputs their feet/COM force/position directly. A small amount of lightweight kinematics/dynamics retargeting is applied and the entire motion transfer system works with lower delay [13]. This approach allows a rapid and highly dynamic motion transfer. However, it is difficult to count

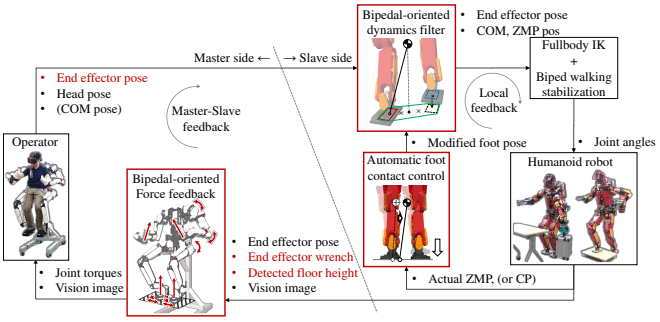

Fig. 3. Schematic diagram showing an overview of the concept of our humanoid robot teleoperation system.

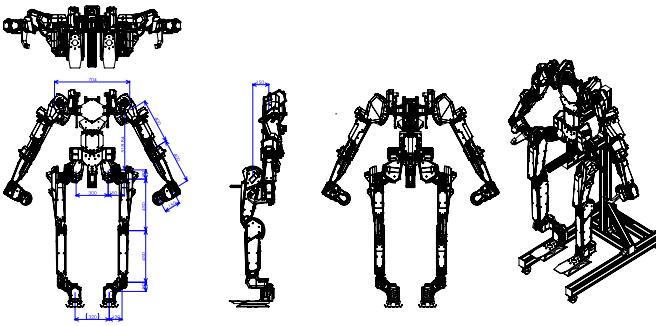

Fig. 4. Various views of TABLIS with/without the base frame.(unit: (mm))

the constraints of the bipedal dynamics online. Therefore, this approach provides higher maneuverability and lower stability. Our main aim is how to tune the maneuvering stability and how to apply a whole-body teleoperation system to a practical task scene.

III. System Overview

A schematic of our bilateral humanoid teleoperation system is shown in Fig. 3. The important features of the teleoperation system are as follows: (1) Normal master-slave feedback loop and local bipedal related feedback loop are coexisting. The local feedback loop plays an important assistive role for bipedal stability. (2) The operator can feel the 3D ground contact information, but this is not reproduced by the 6-DOF slave foot wrench. The vertical ground reaction force of the slave is converted into the "detected floor height," and the operator feels the virtually reproduced floor. In contrast to other normal bilateral control approaches, our approach has several automated subsystems for controlling the bipedal dynamics, and the operator input is treated as a middle-level abstract command. A general bilateral connected two-robot system is composed of a master/slave side hardware/software, and we have worked on the master side hardware (Sec. IV), master side software (Sec. VI), and slave side software (Sec. V). The slave side hardware is the human-scale high-power humanoid robot JAXON [14].

IV. Master Side Hardware

We have adopted the seat-type whole-body exoskeleton cockpit design as shown in Fig. 2(g). The following are the important requirements:

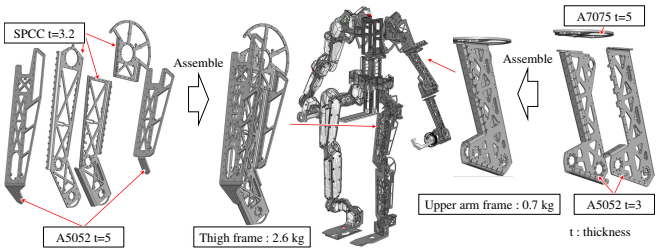

Fig. 5. Sheet metal based frame design of TABLIS

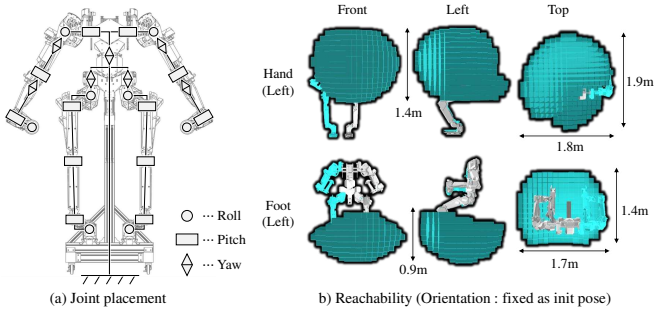

(a) Joint placement

b) Reachability (Orientation : fixed as init pose)

Fig. 6. Joint placement and reachability test

(R1) Maximum continuous torque output of the leg joints. (R2) Joint backdrivability. (R3) Link structure stiffness. (R4) Wide workspace as much as humans. (R5) Less collision with operator body.

There is always a trade-off between (R1) and (R2) and between (R3), (R4), and (R5). In addition, a low-cost, lightweight design is of course preferable. Therefore, we have adopted the following in our design approach:

(A1) Torque-dense motor with active air cooling. (A2) 2-stage gear/pulley reducer and a torque sensorless feedforward torque (current) control. (A3) Sheet metal frame. (A4) Longish limb design. (A5) Kinematic structure is independent from the operator body.

The completed design of our seat-type whole-body exoskeleton cockpit "TABLIS" is shown in Fig. 4. The name "TABLIS" is an acronym for "Teleoperation Assist Bilateral Locomotion Interface Skeleton." The nominal physical specifications of the humanoid exoskeleton part are, mass = 90 kg (upper = 35 kg, lower = 55 kg) and height = 1.9 m. Along with the base frame, these are mass = 124 kg and height = 2.1 m. Fig. 5 shows an example of our sheetmetal-based design and the link mass. The total number of joints is 27 and their placement is designed as shown in the left of Fig. 6. The joint placement has been empirically determined without any ergonomic optimization approach.
Fig. 7 shows our adopted transmission design. Spur gears and timing pulleys are ordinary mechanisms, but they have sufficient transmission efficiency of about 97∼ 99 % [15]. This implies that a combination of the two can provide at least 94 % ($0.97^2 = 0.94$) transmission efficiency, and this can provide much better backdrivability than harmonic drives [16]. A combination of a capstan drive and a current-controlled motor has already been applied to commercial

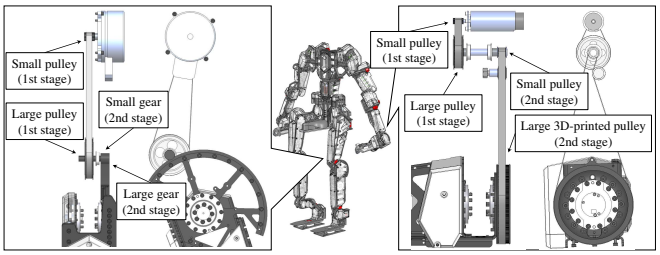

Fig. 7. Different sets of motor and transmission are applied for achieving suitable torque/backdrivability specifications.

TABLE I

NOMINAL CONTINUOUS JOINT TORQUE SPECIFICATIONS.

Joint	Gear ratio 1st×2nd	Motor continuous torque (N m)	Torque (N m)
hip y	4.5×9.0= 40.5	0.533 (flat 90W)	21.6
hip r	4.5×15.0+1= 68.5	0.533 (flat 90W)	36.5
hip p	4.5×15.0+1= 68.5	0.964 (flat 260W)	66.0
knee p	4.5×15.0= 67.5	0.964 (flat 260W)	65.1
ankle p	4.5×9.0= 40.5	0.533 (flat 90W)	21.6
ankle r	4.5×9.0+1= 41.5	0.533 (flat 90W)	22.1
waist y	4.5×15.0= 67.5	0.533 (flat 90W)	36.0
shoulder p	5.14×30.0= 154	0.0952 (4pole 200W)	14.7
shoulder r	5.14×30.0= 154	0.0952 (4pole 200W)	14.7
shoulder y	5.14×20.0= 103	0.0952 (4pole 200W)	9.79
elbow p	5.14×20.0= 103	0.0952 (4pole 200W)	9.79
wrist y	5.14×12.0= 61.7	0.0952 (4pole 200W)	5.88
wrist p	5.14×8.57= 44.1	0.0952 (4pole 200W)	4.20
wrist r	5.14×8.57= 44.1	0.0952 (4pole 200W)	4.20

haptic devices [17] and a combination of a high torque density motor and low gear ratio transmission has been applied recently to a quadruped robot [18]. Our motor/transmission selection policy has been developed by referring to these products. The target joint torque specifications were set based on measured human data [19]. According to the data, the average maximum joint torque values for Japanese males are about (hip, knee, ankle, shoulder, elbow, wrist) = (143, 113, 69, 55, 46, 11) N m. It should be noted that these values are the instantaneous output values for 4∼6 s and therefore cannot be simply compared to the continuous torque values of the robot. As a result, we have achieved a maximum joint torque from a human of 15∼57 %, as shown in Tab. I. MAXON EC 90 flat 90W (flat 90W) and EC 90 flat 260W (flat 260W) motors for the legs and EC-4pole 30 200W (4pole 200W) for the arms were employed.

Tab. II shows an evaluation of the nominal rotor inertia that includes the motor rotor and the 1st stage pulley/shaft. These inertia values indicate the joint inertial resistance against backdrivability. In practice, there exists an inertial resistance, a frictional resistance, and a link inertia resistance. Therefore, we first prepared a unit prototype of the hip p link and checked that the influence of these resistance components was not considerable in the haptic device for legs. In addition, forced air cooling systems were applied to the critical joints (hip roll, hip pitch, knee pitch), as shown in Fig. 8. We inserted a thermometer IC on the coil winding and drilled holes into the outer rotor housing. This method enabled us to boost the continuous motor torque without

TABLE II

NOMINAL JOINT ROTOR INERTIA SPECIFICATIONS.

Joint	Pulley and shaft I×2nd (gcm^2)	Motor I×(1st×2nd) (gcm^2)	Total (gcm^2)
hip y	549×9.0 = 4941	3060×40.5 = 123930	128871
hip r	549×15.0 =8235	3060 ×68.5 = 209610	217845
hip p	549×15.0 = 8235	5060×68.5 = 346610	354845
knee p	549×15.0 = 8235	5060×67.5 =341550	349785
ankle p	549×9.0 = 4941	3060×40.5 = 123930	128871
ankle r	549×9.0 = 4941	3060×41.5 = 126990	131931
waist y	549×15.0 = 8235	3060×67.5 = 206550	214785
shoulder p	143×30.0 = 4290	33.3×154 = 5138	9428
shoulder r	143×30.0 = 4290	33.3×154 = 5138	9428
shoulder y	143×20.0 = 2860	33.3×103 = 3425	6285
elbow p	143×20.0 = 2860	33.3×103 = 3425	6285
wrist y	143×12.0 = 1716	33.3×61.7 = 2055	3771
wrist p	143×8.57 = 1226	33.3×44.1 = 1468	2694
wrist r	143×8.57 = 1226	33.3×44.1 = 1468	2694

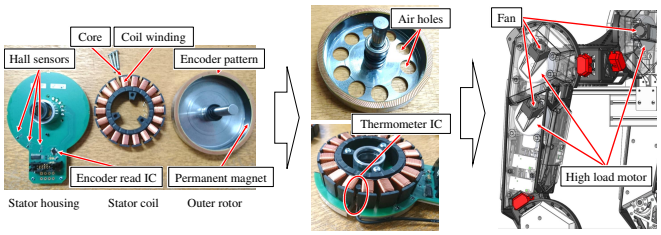

Fig. 8. Modifications for monitoring the coil temperature/forced air cooling.

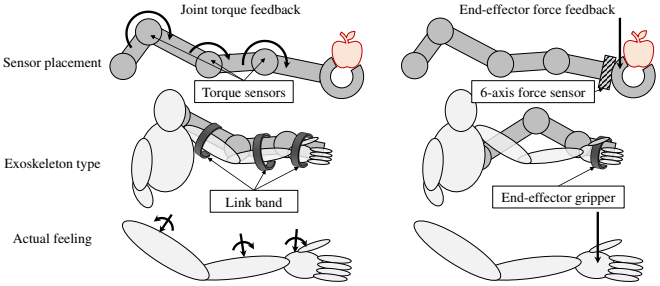

Fig. 9. Difference between an attached-type (L) and independent-type (R).

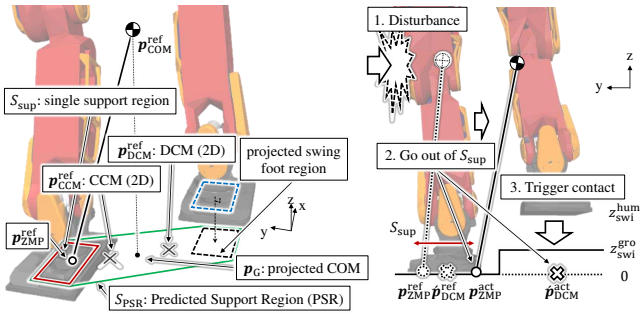

Fig. 10. Bipedal-oriented stability assist based on COM, ZMP, DCM/CCM and predicted support region.

increasing the weight/inertia.

In the case of the whole-body frame, an independent-type exoskeleton design has been adopted for TABLIS. The left panel of Fig. 9 shows the well-known attached-type exoskeleton that is often used in power assist applications. The independent-type exoskeleton is shown in the right panel of Fig. 9, and the DLR-HUG system is an example of this type of exoskeleton [7]. The link placement in this type is almost independent of the operator body, and its kinematics structure and operator's one are quite different. For its employment as a haptic device, the attached-type is not suitable because the feedback force from the end-effector is distributed and the actual force felt will be undesirable, as shown in the left panel figure in the bottom row in Fig. 9. In addition, the independent-type has good operability such that we can easily ride off/on it and pause/resume operation. One of the difficulties in the case of an independent-type exoskeleton is achieving a high stiffness and low inertia. We simulated the stiffness using the finite element method (FEM) available in CAD software and checked if the leg end-effector displacement was under 2 cm with 500 N loads in the X,Y, and Z-directions (considering that every joint is locked ideally). Link inertia can be effectively reduced by relocating the heavy components (motors, circuit boards, gears) close to the root link, and in such design, wire transmissions are often used to actuate the terminal links. We have not adopted such a low inertia design approach because of design complexity and high costs. However, we tried to place the motors and the motor drivers as close as possible to the root link and also applied 3D printed resin parts at the end of the arms. The right of Fig. 6 shows the result of the reachability test of TABLIS. As the result, we can see this frame kinetics has enough workspace for humans.

V. SLAVE SIDE SOFTWARE

A. *Bipedal-oriented dynamics filter*

This feature is the same as our previous work [1], and thus we simply explain it here in brief. We have assumed a simple 2D LIP model (Fig. 10 left) and have used several parameters associated with it, namely, center-of-mass (COM), zero moment point (ZMP) [20], and divergent component of motion (DCM) / convergent component of motion (CCM) [21]. Next, we define the "predicted support region (PSR)" that is formed from the convex hull of both the projected sole regions onto the ground and it is always formed with both feet even if one foot is in the air. We expect that this region will be the double leg support region if the swing leg touches down in the next moment and therefore call it the "predicted" support region. In the 2D plane motion, DCM is also known as the capture point (CP) [22] and is often used as a braking point of the COM motion. Our strategy is to regulate the DCM and CCM inside the PSR. Theoretically, CCM is not used for the stability condition, but we used it to generate a more conservative reference trajectory of the COM. The DCM and CCM can be easily calculated as below.

$$\boldsymbol{p}_{\mathrm{DCM}} := \boldsymbol{p}_{\mathrm{G}} + \dot{\boldsymbol{p}}_{\mathrm{G}}(\sqrt{h/g} + T_{\mathrm{d}}) \quad (T_{\mathrm{d}} := h_{\mathrm{f}}/V_{\mathrm{f}}^{\max}) \tag{1}$$

$$\boldsymbol{p}_{\mathrm{CCM}} := \boldsymbol{p}_{\mathrm{G}} - \dot{\boldsymbol{p}}_{\mathrm{G}}\sqrt{h/g} \tag{2}$$

It should be noted that we use an extended DCM, $\boldsymbol{p}_{\mathrm{DCM}}$, to compensate for the delay in the swing foot landing, T_{d}. Although the delay time, T_{d}, cannot be calculated exactly, we

estimate it approximately using the current swing foot height, $h_{\rm f}$, and its maximum average vertical velocity, $V_{\rm f}^{\max}$. The final reference COM velocity, $\dot{\boldsymbol{p}}_{\rm G}^{\rm ref}$, is modified by regulating $\dot{\boldsymbol{p}}_{\rm DCM}^{\rm ref}$ and $\boldsymbol{p}_{\rm CCM}^{\rm ref}$ inside the PSR $S_{\rm PSR}$ as follows:

$$\dot{\boldsymbol{p}}_{\rm G}^{\rm ref} \quad s.t. \quad \dot{\boldsymbol{p}}_{\rm DCM}^{\rm ref} \subset S_{\rm PSR} \wedge \boldsymbol{p}_{\rm CCM}^{\rm ref} \subset S_{\rm PSR} \tag{3}$$

In this work, since the COM of the operator is constantly fixed above the seat, the operator feels inconvenient to swing his COM intentionally during the gait. Therefore, we discard the operator COM information and artificially generate a simple COM position command. The artificial reference COM position is switched on the left/right/center of the feet depending on the contact state of the operator's feet. Even if the input COM trajectory is a step-function input, this filter reshapes it into a feasible one. The operator's foot/hand movements are integrated considering which foot is contacting to the virtual floor, and those absolute positions on the virtual floor are calculated like a dead reckoning. By this simplification, the operator does not have to move his COM forward intentionally, but he has to pull in and kick backward the virtual floor to continue moving forward.

B. Automatic foot contact control

This feature is an improved version of our previous work [1]. This method is not a novel approach but is effective in mitigating the human/robot or reference/actual ZMP error. This subsystem monitors $\boldsymbol{p}_{\rm ZMP}^{\rm ref}$, $\boldsymbol{p}_{\rm ZMP}^{\rm act}$, and $\dot{\boldsymbol{p}}_{\rm DCM}^{\rm ref}$. $\boldsymbol{p}_{\rm ZMP}^{\rm ref}$ is a reference ZMP derived from the reference COM state $\boldsymbol{p}_{\rm G}^{\rm ref}$, $\ddot{\boldsymbol{p}}_{\rm G}^{\rm ref}$. $\boldsymbol{p}_{\rm ZMP}^{\rm act}$ is an actual ZMP measured by the robot foot force sensors. $\dot{\boldsymbol{p}}_{\rm DCM}^{\rm ref}$ is an extended DCM derived from the final reference COM state $\boldsymbol{p}_{\rm G}^{\rm ref}$, $\dot{\boldsymbol{p}}_{\rm G}^{\rm ref}$. An actual DCM (generally measured by an inertial measurement unit) could also be a candidate for error detection, but it has not been used in this work. By monitoring these reference/actual variables, this subsystem automatically determines whether the swing foot should land on the ground or not. This process can be represented as follows:

$$z_{\rm swi}^{\rm rob} := \begin{cases} z_{\rm swi}^{\rm hum} (\boldsymbol{p}_{\rm ZMP}^{\rm ref} \subset S_{\rm sup} \wedge \boldsymbol{p}_{\rm ZMP}^{\rm act} \subset S_{\rm sup} \wedge \dot{\boldsymbol{p}}_{\rm DCM}^{\rm ref} \subset S_{\rm sup}) \\ z_{\rm swi}^{\rm gro} (otherwise) \end{cases} \tag{4}$$

Here, $z_{\rm swi}^{\rm rob}$ is the height to which the swing foot is lifted in the target robot motion, $z_{\rm swi}^{\rm hum}$ is the input height of the swing foot due to the human motion, $z_{\rm swi}^{\rm gro}$ is the detected floor height, and $S_{\rm sup}$ is the single foot sole region of the support leg. The right of the Fig. 10 shows the relation of these values. The combination of this feature and the bipedal-oriented dynamics filter Sec. V-A can absorb the difference of the LIP model between the human and the robot, e.g., COM height and shape of the sole region. Furthermore, monitoring the actual ZMP, $\boldsymbol{p}_{\rm ZMP}^{\rm act}$, implies that this process has an actual sensor feedback loop and can absorb unexpected disturbances to some extent. When the floor height detection is enabled, the slave robot starts to use the variable floor height and feedback it to the master side. The detection feature is a simple hysteresis switch driven by the vertical foot force. In this work, the detection threshold is 50 N and

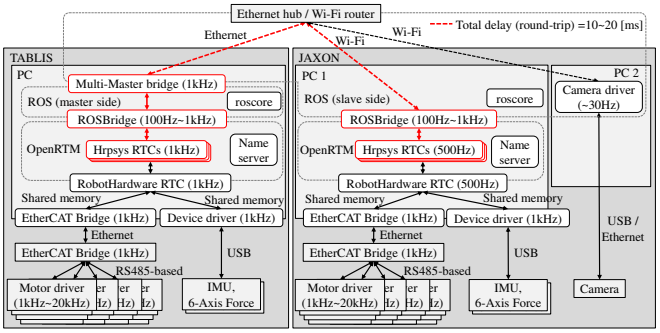

Fig. 11. Connection of the 2 humanoid robot system

the release threshold is = 30 N. 2 s after the release of the floor detection trigger, the current detected floor height is reset to zero. After LIP model-related parameters (i.e., the pose of the feet, COM, ZMP) are decided, we use a biped walking stabilization method [23] that distributes the target ZMP into the two target foot wrenches that are realized by a feet position modification law, similar to an impedance control. After all Cartesian space motion targets (i.e., the pose of the end-effectors, head, COM) are decided, we use the solvability-unconcerned inverse kinematics (IK) [24] to generate the whole-body target joint angles. For the bipedal motion accuracy during the real-time whole-body IK loop, the critical Cartesian space constraints (feet and COM) are set with higher constraint weights, while the others (hands, head) are set with lower constraint weights.

VI. Master Side Software

A. Difficulties of bilateral locomotion and our strategy

Generally, it is said that a sampling rate of over 1 kHz is required to achieve a satisfactory quality of the haptic feeling. However, not only the sampling rate, but also the latency or phase delay is important. Even if both the master and slave robot system are working at 1 kHz, the advantage becomes meaningless when the network has a delay greater than 10 ms. The phase delay factor is not only in the network system, but also in the link structure elasticity, transmission backlash, actuator tracking quality, and so on. These elements cause various oscillation. Furthermore, there is an internal force oscillation problem when a rigid object is inserted between two force-controlled arms [25]. Due to these problematic conditions, it is difficult to achieve a good quality bilateral control system with humanoid robot system as compared to the small-scale bilateral controlled devices. Therefore, we gave up on the direct synchronization of the 6-DOF force/position of the feet of the operator/robot. Our strategy focuses on synchronizing the contact floor surface information that is feedbacked from the slave robot's foot force sensors. However, at present, we have assumed a horizontal uneven floor that we call it a quasi-3D floor. Fig. 11 shows our bilateral humanoid teleoperation system. The master side TABLIS and the slave side JAXON are controlled by the same multi-layered robot control system [26], [27]. Each robot system can operate independently of

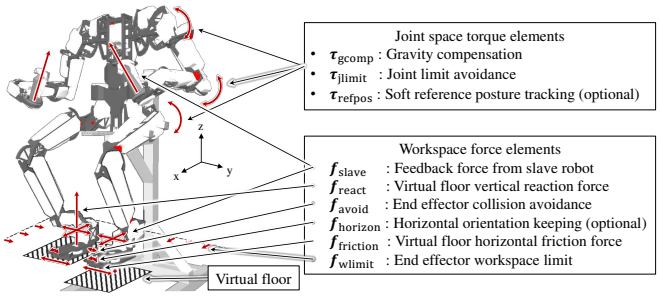

Fig. 12. Force/torque elements included in the torque controller of TABLIS.

the other and each software component runs at 500∼1000 Hz. We have applied a UDP-based ROS connection for the especially important packets for bilateral control. From our preliminary experiment, the sections marked in red color in Fig. 11 have at least 10∼20 ms round-trip connection delay.

B. Bipedal-oriented haptic reproduction

The internal force oscillation can also be a problem on the bilateral controlled bipedal robot. Our approach is adding certain relative constraints between both feet, and this idea is the same as [25]. Therefore our approach can also be categorized as a task-oriented approach. Fig. 12 shows how we control TABLIS as a master device. The hand end-effector has 6-DOF wrench feedback from the slave side, but the foot end-effector is controlled by the quasi-3D floor reproduction instead, and only the F_x and F_y components of force are directly feedbacked. In this quasi-3D floor reproduction, the tilt of the contact floor is assumed to be horizontal and its height is derived from the slave side floor height detection. The virtual floor reaction force is simulated by the penetration into the virtual floor and when both the master feet are in contact with the virtual floor, the inter-locking force is also reproduced. We also applied simple signal shaping to the feedback wrench to suppress any unstable oscillation due to the lack of the gain margin. We have applied a band-stop filter with parameters of the high-pass side having gain = 1 and cutoff = 20 Hz and those of the low-pass side having gain = 0.1 and cutoff = 0.3 Hz. These force/torque elements and other utilities in Fig. 12 can be simply concatenated as Eq. 5:

$$\boldsymbol{\tau}_{\text{total}} = \boldsymbol{\tau}_{\text{gcomp}} + \boldsymbol{\tau}_{\text{jlimit}} + \boldsymbol{\tau}_{\text{refpos}} + \sum_{i=1}^{N_{\text{EE}}} \boldsymbol{J}_i^T ({}^i\boldsymbol{f}_{\text{slave}} + {}^i\boldsymbol{f}_{\text{react}} + {}^i\boldsymbol{f}_{\text{avoid}} + {}^i\boldsymbol{f}_{\text{horizon}} + {}^i\boldsymbol{f}_{\text{friction}}) \quad (5)$$

$\boldsymbol{\tau}_{\text{gcomp}}$ can be calculated by the inverse dynamics. In this study, we have ignored the effect of the joint velocity and acceleration for the sake of simplification. Thus, these values will be the same as the ones from the static equilibrium condition of forces (statics). $\boldsymbol{\tau}_{\text{refpos}}$ is designed to converge the whole-body posture softly to a safe posture under gravity compensation. N_{EE} is the number of end-effectors, which in the present work is 4 (left/right leg/arm). $\boldsymbol{J}_i$ is the Jacobian of the i-th limb, and the size should be (6 of the end-effector twist DOF)×(Number of joints + 6 of the base link DOF), which in the present work is 6×33. In the case where i indicates the left or right hand, the ${}^i\boldsymbol{f}_{\text{react}}$, ${}^i\boldsymbol{f}_{\text{horizon}}$, and ${}^i\boldsymbol{f}_{\text{friction}}$ can be ignored. All force/torque elements without $\boldsymbol{\tau}_{\text{gcomp}}$, ${}^i\boldsymbol{f}_{\text{slave}}$ are designed as simple proportional-derivative control-like law (i.e. spring-damper model). These settings are just an example of ours and there would be room for improvement.

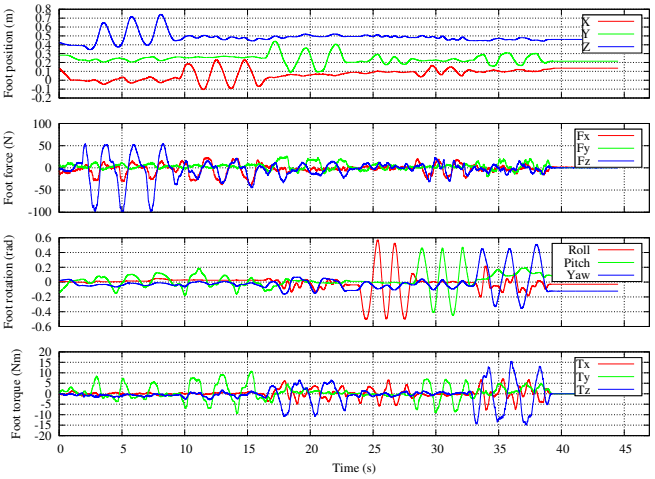

Fig. 13. Assessment of the foot resistance force of the leg part backdrivability (X,Roll:forward, Y,Pitch:Left, Z,Yaw:Up).

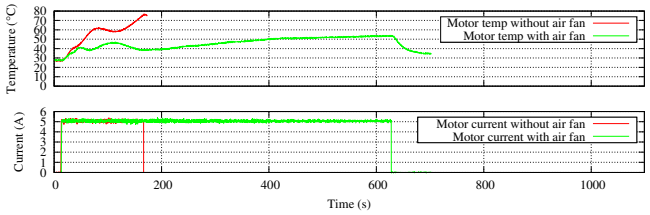

Fig. 14. Coil temperature with and without the air cooling method.

VII. Experiment

A. Evaluation test of TABLIS

The basic performance of the TABLIS design was evaluated with a focus especially on the leg part. The backdrivability assessment is shown in the Fig. 13. A 6-axis force sensor was attached under each foot and swayed along all 6 axes by hand with the gravity compensation activated. Strictly speaking, the backdrivability cannot be assessed easily nor can it be compared, because it contains several factors (such as static/dynamic friction, rotor/link/whole-limb inertia, backlash, cogging torque). Therefore, the results of this experiment show the total tendency of this device. One of the worst results observed is the Z-axis reaction force. In our estimation, the influence of the rotor inertia near the knee-stretched singular pose would be the primary reason for the poor result. The other poor result is observed along the Yaw-axis and is assumed to be due to the influence of the joint placement. The Yaw-axis joint is placed at the root of the whole leg limb, and it is under the large inertial

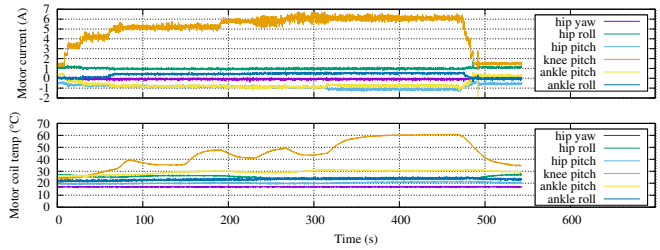

Fig. 15. Motor current and coil temp. (47.5 kgf on the left leg of TABLIS).

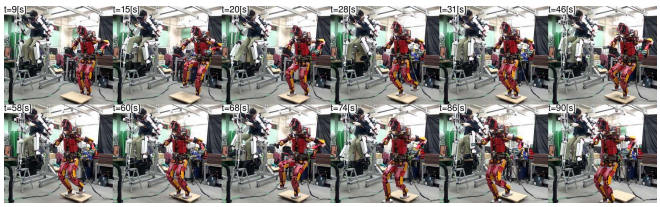

Fig. 16. Images showing the robot traversing an unknown height step using the floor height feedback (step height = 0.07 m).

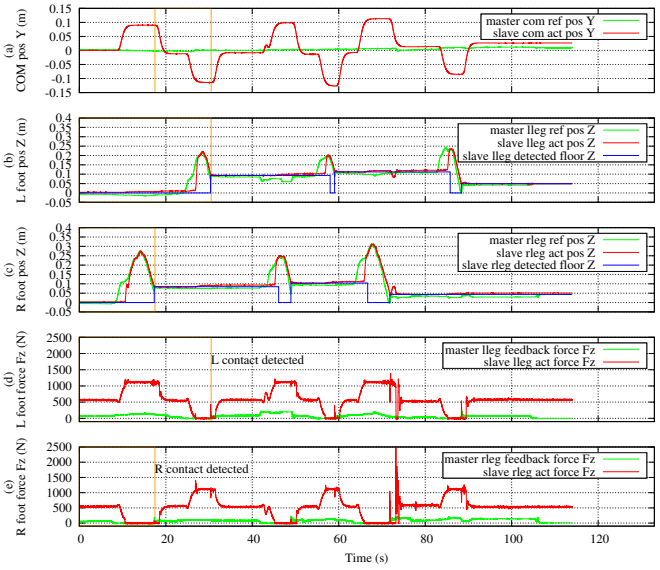

Fig. 17. Plots of the COM, foot height, detected floor height and foot force in the step traverse operation (X,Roll:forward, Y,Pitch:Left, Z,Yaw:Up)

force influence of the whole leg limb. This defect can be solved by adding an extra Yaw-axis joint or redesigning the joint placement. Next, the motor overdrive experiment was conducted. As a preparatory step, the thermo-tolerance of the motor with/without air cooling was surveyed and the results are Fig. 14. The target is MAXON EC 90 flat 260W (maximum continuous current limit: 4 A, coil temperature limit: 120°). With an input current of 5 A without air cooling, its coil temperature was observed to increase dangerously indeed. Next, Fig. 15 shows the results of the load tolerance test of TABLIS. The weights were put on the left sole and the motor current and temperature were monitored. In this pose, the joint with the highest usage is the knee pitch and its applied motor is also MAXON EC 90 flat 260W. Finally, a load of 47.5 kg was kept on its pedal and the motor current was kept at 6 A. The motor coil temperature reached 60°, hitting the peak. From this result, it can be concluded that the implementation of air cooling works well and boosts the effector force.

B. Bilateral 3D locomotion experiment

Fig. 16 and Fig. 17 show the results of the experiment in which we let JAXON traverse over the 7 cm height of the quasi-3D step obstacle using our system. In this experiment, the operator executed 6 footsteps starting from the right foot alternately. The robot stepped on the obstacle (1st, 2nd footstep), moved forward (3rd, 4th footstep), and stepped down from the obstacle (5th, 6th footstep). The height of the obstacle was regarded as unknown and we expected that the floor height detection of the slave robot works and feedbacks it. Fig. 17(a) shows the reference/actual COM position of the master/slave side plotted as a function of time. Fig. 17(b)(c) show the transition of the foot height and slave detected floor height respectively. Fig. 17(d)(e) show the vertical foot force of the master and slave side respectively. In the Fig. 17(a), the master side reference COM (actual operator's COM) is ignored, and the slave side COM tracks the invisible step-shaped reference generated from the master side foot contact state (Sec. V-A). In the Fig. 17(b)(c), even though the actual step height was 7 cm, the actual detected step height was around 10 cm. After stepping down on the ground (7th and 8th footsteps), a drifted value of about 5 cm remained. This could be caused by the influence of the elasticity of the slave leg hardware. However, this is not crucial unless a dead reckoning is carried out with this value. We can also see that the detected floor height is reset to zero at each swing foot phase as designed. In the Fig. 17(d)(e), the floor detection timing corresponds to the small impulse (e.x. orange line). When the impulse force exceeds the floor detection threshold (= 50 N), the detected floor height in (b) or (c) is updated. Since the occurring foot force of the master side is reproduced from the virtual floor, there is no strict relation between the slave actual foot force and master feedback foot force. The waveform of the master feedback foot force depends on how much the operator pushes down the virtual floor. At the 5th footstep (70 $\sim$ 75 s), the slave robot received a large impact from the ground and lost its balance. In this experiment, the slave robot could absorb the impact using the biped walking stabilization [23], but this impact can sometimes damage the hardware.

VIII. Discussion

The limitations of the slave side controller (Sec. V) are, (1) Only the 2D bipedal locomotion has been assumed. Practically, a quasi-3D locomotion such as stair climbing can be executed. However, the difference in the dynamics model has still not been considered. (2) The filtered motion is still dynamic but conservative than the conventional offline locomotion planning approach. This is because an online motion planning strategy cannot access the future information of the feet/COM trajectory, and this feature

degrades the quality of the optimized locomotion trajectory under various locomotion constraints. This disadvantage is fundamental and inevitable. (3) Since the DCM/CCM and COM positions are restricted inside the PSR formed by both legs, the movements of the humanoid robot is inevitably limited to a bipedal motion with a near-standing pose, and the 3D multi-contact case has also not been considered. (4) Automatic foot contact control is only a temporary solution, and it works well only if the ZMP/DCM movement is inside the PSR. When the actual DCM movement unexpectedly goes outside PSR, the disturbance of the influence cannot be dealt with. About the master side controller (Sec. VI), We have abandoned the direct feedback of f_{z}, τ_{x}, and τ_{y} to avoid the bipedal instability. About the master side hardware (Sec. IV), the seat-type cockpit design assumes ordinary task operations with a near-standing pose.

Next, we discuss future prospects and improvements. It is possible to generalize the bipedal-oriented dynamics filter (Sec. V-A) to the modern model predictive control (MPC) [28] The use of CP (DCM in our case) can be regarded as a short-term prediction of the COM goal, and restriction by the PSR can be regarded as a constraint condition of the constrained optimization problems. These limitations and the generated reference trajectories are sequentially updated in every control loop. This is similar to the MPC feature. Therefore, our current strategy could be characterized as a bipedal-oriented lightweight MPC. The automatic foot contact control (Sec. V-B) can be replaced by the richer push-recovery solutions.As mentioned in Sec. VII-B, the floor height detection is not completely reliable yet. The precision of the floor detection depends on the precision of the foot force sensor and lower body stiffness, and the impact of the floor contact depends on the hardness of the slave robot's sole. We will reduce the influence of the floor contact by a hardware damper mechanism under the sole or by acquiring a torque-controlled humanoid robot. TABLIS uses a prototype hardware design (Sec. IV). Regardless of the cost, metal 3D printing is more suitable for the link structure to reduce inertia and improve stiffness, and a harmonic drive actuator module with torque sensor can achieve both high backdrivability and torque. Currently, our system is specialized for bipedal locomotion, but it is possible to extend its applicability to quadruped locomotion, car driving, swimming, etc., if we implement those task-oriented mode.

IX. Conclusion

In this study, we have proposed a system configuration for the bilateral teleoperation of humanoid robots. Our whole software/hardware system design enables infinite locomotion with the operator seated in it, and reproduces a quasi-3D floor environment and partial force feedback. During the experiment, a slave robot was able to traverse a 7 cm height step using the proposed bilateral whole-body teleoperation system. The success rate is still low because the hardware is not tolerant to impact. Our system tuning technique can contribute to the basis for 3D bilateral humanoid teleoperations.

References

[1] Y. Ishiguro *et al.*, "High speed whole body dynamic motion experiment with real time master-slave humanoid robot system," in *IEEE International Conference on Robotics and Automation*, 2018.

[2] A. Brygo *et al.*, "Humanoid robot teleoperation with vibrotactile based balancing feedback," in *International Conference on Human Haptic Sensing and Touch Enabled Computer Applications 2014*.

[3] K. Darvish *et al.*, "Whole-body geometric retargeting for humanoid robots," in *Humanoids*, 2019, pp. 679–686.

[4] R. P. Darken *et al.*, "The omni-directional treadmill: a locomotion device for virtual worlds," in *UIST*, 1997, pp. 213–221.

[5] H. Iwata *et al.*, "Gait master: A versatile locomotion interface for uneven virtual terrain," in *IEEE Virtual Reality 2001*, pp. 131–137.

[6] A. Tobergte *et al.*, "The sigma. 7 haptic interface for mirosurge: A new bi-manual surgical console," in *IROS*, 2011, pp. 3023–3030.

[7] T. Hulin *et al.*, "The dlr bimanual haptic device with optimized workspace," in *ICRA*, 2011, pp. 3441–3442.

[8] L. Peternel *et al.*, "Learning of compliant human–robot interaction using full-body haptic interface," *Advanced Robotics*, vol. 27, no. 13, pp. 1003–1012, 2013.

[9] J. Ramos *et al.*, "A balance feedback interface for whole-body teleoperation of a humanoid robot and implementation in the HERMES system," in *Humanoids2015*, pp. 844–850.

[10] S. Kim *et al.*, "Stable whole-body motion generation for humanoid robots to imitate human motions," in *IROS*, 2009, pp. 2518–2524.

[11] N. E. Sian *et al.*, "Whole body teleoperation of a humanoid robot-development of a simple master device using joysticks," in *IROS*, vol. 3, 2002, pp. 2569–2574.

[12] J. Oh *et al.*, "Real-time humanoid whole-body remote control framework for imitating human motion based on kinematic mapping and motion constraints," *Advanced Robotics*, vol. 33, no. 6, pp. 293–305, 2019.

[13] J. Ramos *et al.*, "Dynamic locomotion synchronization of bipedal robot and human operator via bilateral feedback teleoperation," *Science Robotics*, vol. 4, no. 35, 2019.

[14] K. Kojima *et al.*, "Development of life-sized high-power humanoid robot jaxon for real-world use," in *Humanoids*, 2015, pp. 838–843.

[15] N. E. Anderson *et al.*, "Comparison of spur gear efficiency prediction methods," ARMY RESEARCH AND TECHNOLOGY LABS CLEVELAND OH PROPULSION LAB, Tech. Rep., 1983.

[16] I. Schafer *et al.*, "Space lubrication and performance of harmonic drive gears," in *ESMATS 2005*, vol. 591, pp. 65–72.

[17] T. H. Massie *et al.*, "The phantom haptic interface: A device for probing virtual objects," in *symposium on haptic interfaces for virtual environment and teleoperator systems*, vol. 55, no. 1, 1994, pp. 295–300.

[18] P. M. Wensing *et al.*, "Proprioceptive actuator design in the mit cheetah: Impact mitigation and high-bandwidth physical interaction for dynamic legged robots," *IEEE T-RO*, vol. 33, no. 3, pp. 509–522, 2017.

[19] National Institute of Technology and Evaluation of JAPAN, "Data book of human physical characteristics among healthy japanese (extremity joint torque)."

[20] M. Vukobratović *et al.*, "On the stability of anthropomorphic systems," *Mathematical biosciences*, vol. 15, no. 1-2, pp. 1–37, 1972.

[21] T. Takenaka *et al.*, "Real time motion generation and control for biped robot - 1st report: Walking gait pattern generation-," *IROS2009*, pp. 1084–1091.

[22] J. Pratt *et al.*, "Capture Point: A Step toward Humanoid Push Recovery," in *Humanoids2006*, pp. 200–207.

[23] S. Kajita *et al.*, "Biped walking stabilization based on linear inverted pendulum tracking," in *IROS2010*, pp. 4489–4496.

[24] T. Sugihara, "Solvability-unconcerned inverse kinematics by the levenberg–marquardt method," *IEEE T-RO 2011*, vol. 27, no. 5, pp. 984–991.

[25] K. Kosuge *et al.*, "Task-oriented control of single-master multi-slave manipulator system," *Transactions of the SICE 1994*, vol. 30, no. 7, pp. 793–801.

[26] Y. Kakiuchi *et al.*, "Development of Humanoid Robot System for Disaster Response Through Team NEDO-JSK's Approach to DARPA Robotics Challenge Finals," in *Humanoids2015*, pp. 805–810.

[27] F. Sugai *et al.*, "Design of tiny high-power motor driver without liquid cooling for humanoid jaxon," in *Humanoids2018*, pp. 1059–1066.

[28] C. E. Garcia *et al.*, "Model predictive control: theory and practice—a survey," *Automatica*, vol. 25, no. 3, pp. 335–348, 1989.